IEEE TRANSACTIONS ON ROBOTICS

Modeling of Fluidic Prestressed Composite Actuators With Application to Soft Robotic Grippers

Yitong Zhou, Leon M. Headings ¹⁰, and Marcelo J. Dapino ¹⁰

Abstract—Soft and continuously controllable grippers can be assembled from fluidic prestressed composite (FPC) actuators. Due to their highly deformable features, it is difficult to model such actuators for large deflections. This article proposes a new method for modeling large deflections of FPC actuators called the chained composite model (CCM) to characterize the quasi-static response to an applied fluid pressure and load. The CCM divides an FPC actuator into discrete elements and models each element by a small rotation model. The strain energy of each element and the work done by pressure and loads are computed using third-order displacement polynomials with unknown coefficients; then, the total energy is minimized to calculate stable shapes using the Rayleigh-Ritz method. This study provides a set of systematic design rules to help the robotics community create FPC actuators by understanding how their responses vary as a function of input forces and pressures for a number of modeling and design parameters. Composite actuators are fabricated and a soft gripper is developed to demonstrate the grasping ability of the FPC actuators. Pneumatic pressure and end loads are applied to the composite actuators, and their responses are measured. The modeled responses of the actuators are shown to be in agreement with the measured responses.

Index Terms—Hydraulic/pneumatic actuators, laminated composites, soft robotic applications, soft robot materials and design.

I. INTRODUCTION

OFT robotics exhibit relatively high compliance, continuum body motion, and large-scale deformation compared to rigid robots. Such characteristics enable soft robots to perform highly dexterous tasks [1], tackle uncertainties with passive compliance [2], manipulate delicate objects [3], and cooperate safely with humans [4].

Manuscript received May 18, 2021; revised September 26, 2021; accepted November 30, 2021. This paper was recommended for publication by Associate Editor C. Rucker and Editor A. Menciassi upon evaluation of the reviewers' comments. This work was supported in part by the National Science Foundation (NSF) through the National Robotics Initiative under Grant CMMI-1637656 and in part by the Smart Vehicle Concepts Center, a Phase III National Science Foundation Industry–University Cooperative Research Center under Grant NSF IIP 1738723. (Corresponding author: Marcelo J. Dapino.)

Yitong Zhou was with the Department of Mechanical and Aerospace Engineering, The Ohio State University, Columbus, OH 43210 USA. She is now with the Shien-Ming Wu School of Intelligent Engineering, South China University of Technology, Guangzhou 511442, China (e-mail: zhouyitong@scut.edu.cn).

Leon M. Headings and Marcelo J. Dapino are with the Department of Mechanical and Aerospace Engineering, The Ohio State University, Columbus, OH 43210 USA (e-mail: headings.4@osu.edu; dapino.1@osu.edu).

Color versions of one or more figures in this article are available at https://doi.org/10.1109/TRO.2021.3139770.

Digital Object Identifier 10.1109/TRO.2021.3139770

Many soft robots have been developed utilizing various kinds of mechanisms, such as a universal robotic gripper using granular jamming [5], a starfish-like gripper based on embedded pneumatic networks [6], a hydraulically actuated soft robot fish [7], and a variable stiffness robotic arm based on discrete layer jamming [8]. Among these, fluidic elastomer actuators (FEAs) are one of the most widely adopted technologies for soft robotics due to their light weight, high power-to-weight ratio, low material cost, and ease of fabrication [9], [10]. Actuation is achieved through pressure exerted by a fluid (liquid or gas) on a chamber made of highly deformable materials, such as silicone rubber. Upon pressurization, embedded chambers in the soft actuator expand in the directions associated with low stiffness and induce bending [6], twisting [11], and extension or contraction [12]. Furthermore, these actuators can be integrated into the structure of soft robotic systems both as actuators and structural elements [3], [6], [12], [13].

A fluid-actuated precurved soft actuator is a type of FEA that has a curvature in its equilibrium unactuated state. Upon actuation, the precurved actuator becomes flat. When used in a gripper, this allows it to open. Releasing the actuation returns the actuator to its equilibrium curved state, hence allowing for grasping of objects in the gripper. An advantage of precurved actuators is that they require no energy to hold an object. Ho and Hirai [14] presented a soft gripper composed of fingers with prestreched soft layers, where each finger's curvature is controlled by a simple tendon string pulled/released by a single actuation. However, a complex integration of motors, tendons, and spools is needed, which can result in a bulky system. Li et al. [15] designed a soft bending actuator that is actuated to a curved equilibrium shape by a precharged air pressure and retracted by inextensible tendons. This method requires both electric and pneumatic actuation to function, which adds complexity to the actuation system. Chillara et al. [16] proposed a fluidic prestressed composite (FPC) actuator, in which a prestressed elastomeric layer is used to generate the curved equilibrium shape and a pneumatic source is used to flatten the actuator. FPC actuators can be easily designed through the selection of properties for each layer. However, the analytical model proposed in [16] only works for small deflections of composite actuators with small and constant curvatures, which inhibits design for gripping applications.

Various models have been developed for the response of FEAs under applied pressures and loads. A brief review of different modeling methods is given in [10], including empirical, analytical, and finite-element methods. Despite achievements

1552-3098 © 2021 IEEE. Personal use is permitted, but republication/redistribution requires IEEE permission. See https://www.ieee.org/publications/rights/index.html for more information.

made via empirical methods [17]–[19], they provide limited insights into the physics of multimaterial FEAs, which limits their potential for design purposes. Finite-element models provide a more detailed and visual description of the nonlinear response of the system, although at the expense of higher computational cost [9], [20], [21]. Analytical modeling methods, on the other hand, offer some advantages over finite-element models, such as providing insights about the physics of the phenomenon and fast computation.

Several pioneering studies have been conducted on analytical modeling for quasi-static responses of different FEA types, the most studied of which are fiber-reinforced FEA [9], [15], [22], [23] and pneu-net FEA [24]. A common challenge in these models is that they assume constant curvature, which is more suitable in the unloaded state but can be inaccurate when the applied moment is not constant along the actuator or the cross section of the actuator is not uniform. In addition, these models cannot be directly applied to FPC actuators.

The piecewise constant-curvature approximation is widely used to model continuum deformable bodies, where the highly nonuniform shape in both 2-D and 3-D can be well simulated. Numerous kinematic studies on continuum robotics have adopted this assumption, mainly for control purposes [25]–[29]. However, fewer efforts have focused on developing material mechanics models, which are more appealing for design purposes than semiempirical models that are based on experimental results.

Inspired by the piecewise constant-curvature method and the small rotation model (SRM), this article presents a method called the chained composite model (CCM) for modeling FPC actuators under large deflections. The CCM segmentizes a composite actuator into multiple elements and models each element using the SRM from [16]. The CCM is developed using a Lagrangian strain description based on classical laminated plate theory and takes material mechanics and geometric nonlinearity into consideration. Low-order polynomial functions with unknown coefficients are used to represent the quasi-static equilibrium shape for each segment of the FPC actuator. The coefficients are calculated by minimizing the system net energy of the FPC actuator in response to the applied fluid pressure and external loads. With the CCM, we investigate the effects of geometric parameters and the number of CCM segments on the modeled responses of FPC actuators. Multiple FPC actuators have been fabricated and experiments have been performed for model validation.

In summary, a large-deflection analytical model has been developed for FPC actuators, which enables analyzing small and large curvatures and constant and nonconstant curvatures. Following a similar process, many other constant-curvature models [9], [15], [22]–[24] can be modified to analyze nonconstant curvatures. The parametric analysis provides a design methodology for designers to select structural parameters and pneumatic pressure to achieve targeted curvatures and gripper flexural rigidity, or to predict bending curvatures and flexural rigidity based on structural parameters, pressures, and applied forces. Motion capture and loading tests have validated the model relating actuator shapes to applied pressures and external

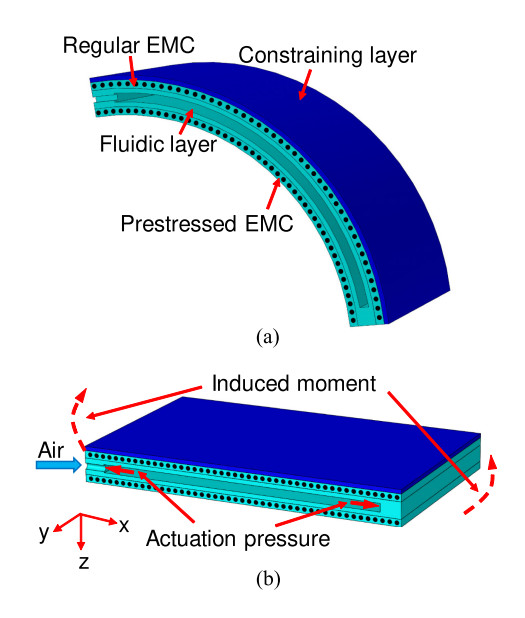


Fig. 1. Rendering of an FPC actuator in its (a) equilibrium curved state and (b) actuated straight state.

loads. Compared to the SRM [16], the CCM eliminates the limitation of small deflections with small and constant curvatures since each segment has its own shape function with a small deflection in its local coordinate frame, but can add up to a large deflection with nonconstant curvature in the actuator's global coordinate frame. This allows for modeling complex loading conditions, such as nonuniform loads and variable cross sections. In addition, low-order polynomials and segmentization allow for fast computation, solving in several seconds depending on the number of segments. Finally, two important design improvements have been made compared to the original actuators from [16]: 1) replacing the metal inlet air tube with a compressed soft tube and 2) adding stiffening ribs to the fluid channel inside the actuator. The former helps to increase the maximum air pressure from 80 kPa to around 400 kPa without air leakage, which allows for flattening FPC actuators with larger initial curvatures, hence providing larger gripper strokes. The latter prevents ballooning under high pressures, hence helping translate the effects of pressure into a moment for changing curvature.

The rest of this article is organized as follows. The FPC actuator mechanism is described in Section II. Section III presents the CCM. Section IV shows parametric studies for design of an FPC. FPC fabrication and a soft gripper are demonstrated in Section V. The fabricated samples are tested for CCM validation in Section VI. Finally, Section VII concludes this article.

II. PRESTRESSED FLUIDIC COMPOSITE ACTUATOR MECHANISM

The concept of a prestressed composite actuator proposed by Chillara *et al.* [16] is shown in Fig. 1. The composite actuator is composed of four layers, including a prestressed elastomeric matrix composite (EMC) layer, a fluidic layer with embedded fluid channels, a regular EMC layer, and a constraining layer.

The equilibrium curved state [see Fig. 1(a)] is created by fabricating the actuator with a prestressed EMC layer. Pneumatically pressurizing the actuator flattens the actuator from a curved state [see Fig. 1(a)] to a flat state [see Fig. 1(b)].

An EMC layer is a fiber-reinforced elastomer composite that exhibits anisotropic stiffness, and its mechanical properties vary with the orientation and volume fraction of the embedded fibers. EMC has fibers oriented along the Y-axis (90°), making it stiff in this direction and compliant in the X-direction [see Fig. 1(b)]. A 90° EMC layer is made by sandwiching the carbon fibers oriented along the Y-axis (90°) between two precured silicone layers. Due to this fiber orientation, the 90° EMC is almost inextensible in the Y-direction and highly compliant in the X-direction. Prestretching a 90° EMC along its X-axis prior to bonding it to other layers creates a precurved actuator in its equilibrium state.

A fluidic layer is an elastomer layer with fluid channels molded in it. To translate the effects of pressure into a moment for changing curvature [see Fig. 1(a)], fluid channels are designed to expand only along the longitudinal direction under pressurization. The Y-direction strain is negligible due to the constraint given by the adjacent EMC layers, whereas the Z-direction strain can be mitigated by adding ribs inside the fluid channels, as described in Section III.

A regular (no prestress) 90° EMC layer is added between the constraining layer and the fluidic layer to constrain the Y-axis expansion when the composite is pressurized.

A constraining layer is typically a thin film with a much higher elastic modulus than that of the other layers. It is used to produce the inextensibility property required for actuation and to increase the actuator's flexural stiffness.

The laminae of the composite actuators can be arranged in different configurations, as shown in [16]. In this article, we chose the configuration shown in Fig. 1 since it generates a large curvature for a given prestrain, which yields a large gripper stroke from curved to flat. More details about different configurations can be found in [16].

III. LARGE ROTATION MODEL FOR COMPOSITE ACTUATORS—CCM

The CCM presented in this article segmentizes the composite along its X-axis into a few elements and models each element using the SRM. Each element of the composite is modeled as a laminated plate based on a strain formulation and classical laminate theory. Strain energy for each segment and actuation work are computed using third-order displacement polynomials with unknown coefficients. Energy minimization is carried out using the Rayleigh–Ritz method, and the polynomial coefficients are solved for the displacements of each segment. By using the CCM, the composite actuator's curvatures and flexural rigidity are analyzed and derived from structural parameters (material properties and actuator geometries), pneumatic pressures, and external forces.

A. Structures and Geometries

Fig. 2 shows our proposed composite actuator. The four layers, including a prestressed EMC layer, a fluidic layer with

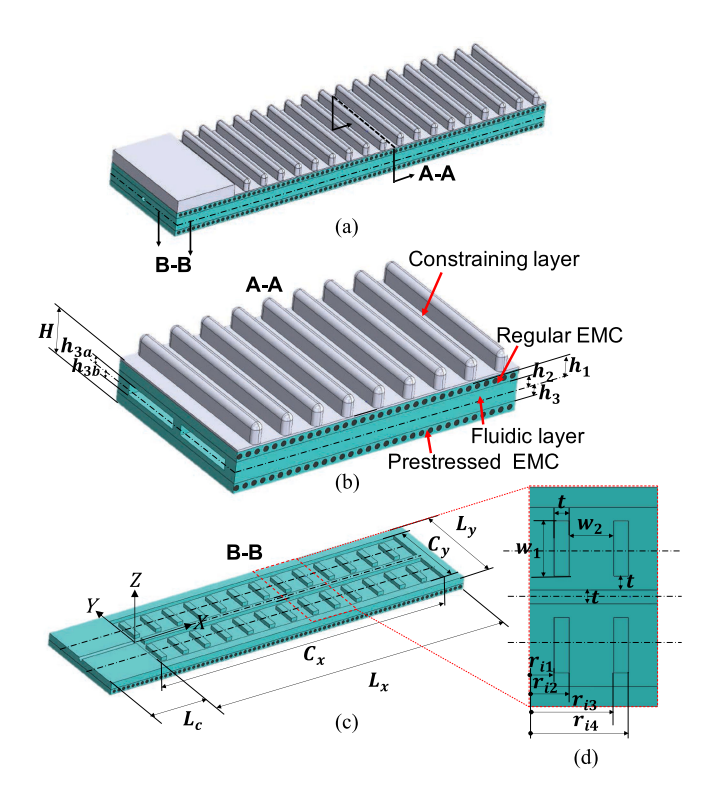


Fig. 2. Proposed design and geometry for an FPC actuator. (a) Overall view. (b) Section view A-A. (c) Section view B-B, at the midplane. (d) *i*th segment of the fluidic layer.

embedded fluid channels, a regular EMC layer, and a constraining layer, are indicated in Fig. 2(b). Compared to the original design in [16], we propose two main changes to improve the actuator performance: 1) for the constraining layer, stiffening ribs are added to prevent bulging of the constraining layer under high pressure, which could cause an uneven stressed interface between the constraining layer and the regular EMC layer, further damaging the interface adhesive; and 2) for the air channel, transverse ribs in the Y-direction and a longitudinal rib in the X-direction are added to connect the top and bottom surfaces of the fluidic layer to prevent ballooning in the Z-direction under pressure, hence helping translate the effects of pressure into a moment for changing curvature. This phenomenon was also noticed in [17] when comparing cylindrical, ribbed, and pleated soft actuators.

The coordinate frame for a composite actuator is defined in Fig. 2(c), where the coordinate origin is L_c from the tip of the actuator. Note that L_c corresponds to the length that is clamped flat by a base fixture. The XY plane is the midplane of the composite actuator, as indicated in Fig. 2(a), using a dashed-dotted line, which is at the middle of the actuator height. The XZ plane is at the middle of the actuator width. Geometric parameters of the composite actuator are shown in Fig. 2(b) and (c) and include the following: composite length L_x , width L_y , and height H; fluid channel length C_x and width C_y ; and out-of-plane heights of each layer with respect to the composite midplane h_1, h_2, h_3, h_{3a} , and h_{3b} . In addition, fluidic layer ribs in the Y-direction have width w_1 , length t, and between-ribs spacing w_2 , as shown in Fig. 2(d). For the fluidic layer, the

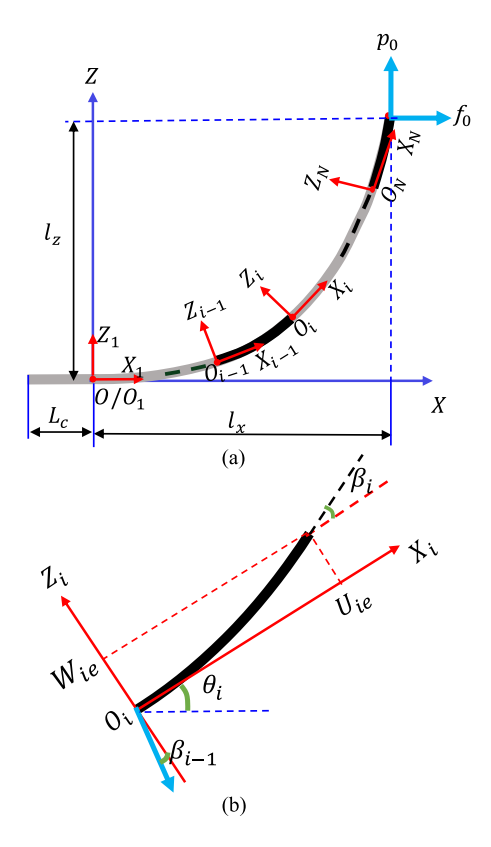


Fig. 3. (a) Segmentization of a composite at its deflected equilibrium state. (b) *i*th segment at its deflected equilibrium state.

spacing between the transverse and longitudinal ribs and the width of longitudinal ribs are both t [see Fig. 2(d)].

B. Segmentization

Fig. 3(a) shows the midplane of a curved composite, where the composite is segmentized into N segments, and for the ith segment shown in Fig. 3(b), its local coordinate frame $(O_iX_iZ_i)$ is attached to and moves along with the free end of the (i-1)th element, i.e., O_i . The first segment's coordinate frame $(O_1X_1Z_1)$ coincides with the global coordinate frame (OXZ), which is the same as in Fig. 2(c). The length of each segment before deflections and prestress is denoted L_i . The end rotation angle for the ith segment is denoted β_i . The angle between OX_i and OX at each node O_i is denoted θ_i , which can be expressed with respect to end rotation angles from all previous segments as

$$\theta_i = \sum_{k=1}^{i-1} \beta_k \ (i \in [2, ..., N]), \quad \theta_1 = 0.$$
 (1)

Forces f_0 and p_0 are applied along X and Z, respectively, to the free end of the composite. A rule of thumb for small end rotation angles is given by [30] as $\frac{\partial w_0}{\partial x} < 1$, which corresponds to approximately $\beta_i < 45^\circ$. For example, to model the whole composite illustrated in Fig. 3(a), which has an end rotation angle of approximately 90° , at least two elements would be required.

C. Strain Energy of the ith Segment

Strain energy modeling of the *i*th segment follows the small rotation modeling presented in [16]. The strain of the midplane

of the actuator is represented using polynomial functions with unknown coefficients. We first describe midplane displacements of the ith segment of the composite in the X_i , Y_i , and Z_i directions by polynomial functions with unknown coefficients as

$$u_{i0} = b_{i1}x + b_{i3}x^3, \ v_{i0} = c_{i1}y, \ w_{i0} = d_{i2}x^2$$
$$(x \in [0, L_i], \ y \in [-L_y/2, L_y/2], \ i \in [1, ..., N])$$
(2)

where the subscripts i and 0 denote the ith segment and the midplane, respectively. The strains $(\epsilon_{xx}, \gamma_{xy}, \epsilon_{yy})$ of an arbitrary point (x, y, z) on the ith segment of the composite are expressed in terms of its displacements (u_{i0}, v_{i0}, w_{i0}) as [31]

$$\epsilon_{ix} = \frac{\partial u_{i0}}{\partial x} + \frac{1}{2} \left(\frac{\partial w_{i0}}{\partial x} \right)^2 - z \left(\frac{\partial^2 w_{i0}}{\partial^2 x} \right)$$

$$\epsilon_{iy} = \frac{\partial v_{i0}}{\partial y} + \frac{1}{2} \left(\frac{\partial w_{i0}}{\partial y} \right)^2 - z \left(\frac{\partial^2 w_{i0}}{\partial^2 y} \right)$$

$$\gamma_{ixy} = \frac{\partial u_{i0}}{\partial y} + \frac{\partial v_{i0}}{\partial x} + \frac{\partial w_{i0}}{\partial x} \frac{\partial w_{i0}}{\partial y} - 2z \left(\frac{\partial^2 w_{i0}}{\partial x \partial y} \right). \tag{3}$$

By substituting (2) into (3), one obtains

$$\epsilon_{ix} = 2d_{i2}^2x^2 - 2zd_{i2} + 3b_{i3}x^2 + b_{i1}$$

$$\epsilon_{iy} = c_{i1}$$

$$\gamma_{ixy} = 0.$$
(4)

Transverse shear (XZ, YZ) and transverse normal (ZZ) stresses are neglected due to the plane stress assumption of classical laminated plate theory. Hence, the strain energy of the constraining layer for the ith segment can be written as

$$\Phi_{\text{CL}(i)} = \int_{h_1}^{H/2} \int_{-Ly/2}^{Ly/2} \int_{0}^{L_i} \left(\frac{1}{2} Q_{11}^{(\text{CL})} \epsilon_{ix}^2 + Q_{12}^{(\text{CL})} \epsilon_{ix} \epsilon_{iy} + \frac{1}{2} Q_{22}^{(\text{CL})} \epsilon_{iy}^2 \right) dx dy dz \quad (5)$$

where Q_{pq} are the plane stress-reduced stiffnesses given as

$$Q_{11} = \frac{E_1}{1 - \nu_{12}\nu_{21}}, \ Q_{12} = \frac{\nu_{12}E_2}{1 - \nu_{12}\nu_{21}}, \ Q_{22} = \frac{E_2}{1 - \nu_{12}\nu_{21}}$$
(6)

where E and ν are the elastic modulus and Poisson's ratio of each lamina, respectively. An initial finite-element analysis showed that the strain energy stored in the ribs is much smaller than that stored in the thin region; hence, the thickness of the constraining layer is assumed to be constant.

The strain energy of the regular EMC layer $\Phi_{\rm EMC}$ has the same energy form as in (5) except for replacing $Q_{pq}^{\rm (CL)}$ with $Q_{pq}^{\rm (EMC)}$ and integrating over $[h_2,h_1]$ along the Z-axis.

The strain energy of the prestressed EMC layer with a prestrain of ϵ_0 for the *i*th segment is expressed as

$$\Phi_{\text{PEMC}(i)} = \int_{-H/2}^{-h_3} \int_{-Ly/2}^{Ly/2} \int_{0}^{L_i} \left(\frac{a_1}{5} (\epsilon_0 - \epsilon_{ix})^5 + \frac{a_2}{4} (\epsilon_0 - \epsilon_{ix})^4 + \frac{a_3}{3} (\epsilon_0 - \epsilon_{ix})^3 + \frac{a_4}{2} (\epsilon_0 - \epsilon_{ix})^2 + \frac{1}{2} Q_{22}^{(\text{EMC})} \epsilon_{iy}^2 \right) dx dy dz \quad (7)$$

TABLE I

POLYNOMIAL COEFFICIENTS CORRESPONDING TO A NONLINEAR STRESS FUNCTION FOR A 90° EMC MADE OF CARBON FIBER-REINFORCED SILICONE, OBTAINED FROM A UNIAXIAL TENSILE TEST [16]

where the coefficients a_i (i = 1, 2, 3, 4) are those of a quartic polynomial that describes the nonlinear stress function for a 90° EMC [16] listed in Table I.

The strain energy of the fluidic layer for the *i*th segment is expressed as

$$\Phi_{\text{FL}(i)} = \Phi_{\text{whole}(i)} - \Phi_{\text{channel}(i)} + \Phi_{\text{ribs}(i)} \tag{8}$$

where $\Phi_{\mathrm{whole}(i)}$, $\Phi_{\mathrm{channel}(i)}$, and $\Phi_{\mathrm{ribs}(i)}$ are the strain energies for the whole volume, the channel volume without ribs, and ribs of the fluidic layer on the ith segment, respectively. The strain energy of the whole volume of the fluidic layer for the ith segment is calculated as

$$\Phi_{\text{whole}(i)} = \int_{-h_3}^{h_2} \int_{-Ly/2}^{Ly/2} \int_{0}^{L_i} \left(\frac{1}{2} Q_{11}^{(\text{FL})} \epsilon_{ix}^2 + Q_{12}^{(\text{FL})} \epsilon_{ix} \epsilon_{iy} + \frac{1}{2} Q_{22}^{(\text{FL})} \epsilon_{iy}^2 \right) dx dy dz. \tag{9}$$

The strain energy of the channel volume of the fluidic layer without ribs for the *i*th segment is calculated as

$$\begin{split} \Phi_{\text{channel}(i)} &= \int_{-h_{3b}}^{h_{3a}} \int_{-Cy/2}^{Cy/2} \int_{0}^{C_{ix}} \left(\frac{1}{2} Q_{11}^{(\text{FL})} \epsilon_{ix}^2 + Q_{12}^{(\text{FL})} \epsilon_{ix} \epsilon_{iy} \right. \\ & + \left. \frac{1}{2} Q_{22}^{(\text{FL})} \epsilon_{iy}^2 \right) \! dx dy dz \end{split} \tag{10}$$

where C_{ix} is the length of the fluid channel for the *i*th segment. The strain energy of the ribs inside the fluid channel for the *i*th segment is expressed as

$$\begin{split} \Phi_{\text{ribs}(i)} &= \int_{-h_{3b}}^{-h_{3a}} \int_{-t/2}^{t/2} \int_{0}^{C_{ix}} \\ &\times \left(\frac{1}{2} Q_{11}^{(\text{FL})} \epsilon_{ix}^{2} + Q_{12}^{(\text{FL})} \epsilon_{ix} \epsilon_{iy} + \frac{1}{2} Q_{22}^{(\text{FL})} \epsilon_{iy}^{2} \right) dx dy dz \\ &+ \int_{-h_{3b}}^{-h_{3a}} 2 \int_{3t/2}^{3t/2 + w_{1}} \sum_{j=1}^{n_{i}-1} \int_{r_{ij}}^{r_{i(j+1)}} \\ &\times \left(\frac{1}{2} Q_{11}^{(\text{FL})} \epsilon_{x}^{2} + Q_{12}^{(\text{FL})} \epsilon_{x} \epsilon_{y} + \frac{1}{2} Q_{22}^{(\text{FL})} \epsilon_{y}^{2} \right) dx dy dz, \\ &j <= n_{i} - 1, \ j \in [1, 3, 5, \ldots] \end{split}$$

where the first and second blocks represent the strain energy of the longitudinal rib in the X-direction and all small ribs in the Y-direction. If there are no transverse ribs inside the ith segment, the second block is zero. It is noted that the number of rib nodes on the ith segment in the X-axis is n_i , which is two times the number of ribs in the ith segment. By this definition, n_i is an even number. In addition, r_{ij} is the coordinate of the

jth node in the ith segment along the X-axis. For example, Fig. 2(d) shows the ith segment, where there are two ribs and $n_i=2\times 2=4$ rib nodes in the X-direction with coordinates in the X-direction of $r_{i1},\,r_{i2},\,r_{i3},\,$ and $r_{i4},\,$ in which r_{i1} depends on the initial segmentization for the ith segment, $r_{i2}=r_{i1}+t,\,r_{i3}=r_{i2}+w_2,\,$ and $r_{i4}=r_{i3}+t.\,$ Different segmentization affects the distribution and the number of ribs in the ith segment. Note that the sum of the number of ribs in each segment $\sum_{i=1}^{N}n_i$ does not necessarily equal the total number of ribs in the actuator, because if a transverse rib crosses the ith and (i+1)th segments, that rib accounts for one rib in each segment with their lengths adding to t.

Therefore, the strain energy of the ith segment $\Phi_{(i)}$ can be expressed as the summation of the strain energies of the constraining layer $\Phi_{\text{CL}(i)}$, the regular EMC reinforcement layer $\Phi_{\text{EMC}(i)}$, the prestressed EMC layer $\Phi_{\text{PEMC}(i)}$, and the fluidic layer $\Phi_{\text{FL}(i)}$ as

$$\Phi_{(i)} = \Phi_{\text{CL}(i)} + \Phi_{\text{EMC}(i)} + \Phi_{\text{PEMC}(i)} + \Phi_{\text{FL}(i)}.$$
(12)

D. Chain Rule and Work Done by Loads

Only displacements in the X and Z directions are considered for load analysis due to loads in these directions. The deflected positions are calculated as follows: deflected positions = displacements + original coordinates. For a random point on the ith segment's midplane, its original positions are (x, y, 0) in its local coordinate frame. Note that by the definition of the midplane, the Z_i -direction position of the midplane is 0 before deflection. Based on the displacements in (2) and the original positions, under deflection, the positions of points along the ith segment's midplane in the local coordinate frame are expressed as

$$U_{i0} = u_{i0} + x = (b_{i1} + 1)x + b_{i3}x^{3}$$

$$W_{i0} = w_{i0} + 0 = d_{i2}x^{2}$$

$$(x \in [0, L_{i}], y \in [-L_{y}/2, L_{y}/2], i \in [1, ..., N]). (13)$$

We denote the end position of the ith segment's midplane in the local coordinate frame as

$$U_{ie} = U_{i0}|_{(x=L_i)} = (b_{i1} + 1)L_i + b_{i3}L_i^3$$

$$W_{ie} = W_{i0}|_{(x=L_i)} = d_{i2}L_i^2.$$
(14)

The position of the end of the *i*th segment in the global coordinate frame is

$$\begin{bmatrix} U_{ie}^{0} \\ W_{ie}^{0} \end{bmatrix} = \begin{bmatrix} 1 & 0 & \cos\theta_{i} & -\sin\theta_{i} \\ 0 & 1 & \sin\theta_{i} & \cos\theta_{i} \end{bmatrix} \begin{bmatrix} U_{(i-1)e}^{0} \\ W_{(i-1)e}^{0} \\ U_{ie}^{i} \\ W_{ie}^{i} \end{bmatrix}$$
(15)

where the superscript 0 represents the global coordinate frame and the subscript ie indicates the end position of the ith segment. The expression for θ_i is given in (1), and the end slope of the ith

6

segment β_i is calculated as

$$\beta_{i} = \arctan\left(\frac{dW_{i0}}{dU_{i0}}\right)|_{(x=L_{i})}$$

$$= \arctan\left(\frac{dW_{i0}/dx}{dU_{i0}/dx}\right)|_{(x=L_{i})}$$

$$= \arctan\left(\frac{2d_{i2}L_{i}}{(b_{i1}+1)L_{i}+3b_{i3}L_{i}^{2}}\right). \tag{16}$$

By recursively calling (15), the end position of the Nth segment's midplane in the global coordinate frame $[U^0_{Ne}, W^0_{Ne}]^T$ is expressed in terms of the coefficients for all segments $k_i = (b_{i1}, b_{i3}, c_{i1}, d_{i2})$ and L_i $(i \in [1, \ldots, N])$. Then, the displacement of the Nth segment's midplane in the global coordinate frame is simply calculated as

$$u_{Ne}^{0} = U_{Ne}^{0} - L_{x}, w_{Ne}^{0} = W_{Ne}^{0}$$
(17)

where L_x is the original full length of the composite. Therefore, virtual work done by end loads on the composite actuator, as shown in Fig. 3, is calculated as

$$\delta W_F = f_0 \cdot \delta u_{N_e}^0 + p_0 \cdot \delta w_{N_e}^0. \tag{18}$$

When loads are applied at an intermediate location rather than the free end, one needs to segmentize the actuator before and after the loading point separately. Then, the work term in (18) is computed for the segments only before the loading point.

E. Work Done by Pressure to the ith Segment

The work done by the pneumatic source on the composite's ith segment and the final volume V_{if} of the fluid channel under pressurization for the ith segment are expressed as

$$W_{P(i)} = \frac{P_0 V_{i0} - P_f V_{if}}{\gamma - 1},$$

$$V_{if} = \int_{V_i} (1 + \epsilon_{ix})(1 + \epsilon_{iy}) dV_i, \quad i \in [1, ..., N] \quad (19)$$

where $\gamma=1.4$ is the adiabatic coefficient of air and P_0, P_f, V_0 , and V_f are the initial pressure, final pressure, initial volume, and final volume, respectively, of the air channel during a pressurization process. When actuated, the final volume V_{if} of the fluid channel for the ith segment has the same volume as $\Phi_{\mathrm{channel}(i)} - \Phi_{\mathrm{ribs}(i)}$ and can be integrated in a similar fashion. In addition, the initial pressure P_0 is assumed to be zero since every actuated state can be considered as being actuated from zero pressure, which means we assume a memoryless system. Therefore, the work done by the pneumatic source on the composite's ith segment is simply

$$W_{P(i)} = \frac{-P_f V_{if}}{\gamma - 1} = \frac{-P_f \int_{V_i} (1 + \epsilon_{ix})(1 + \epsilon_{iy}) dV_i}{\gamma - 1}.$$
 (20)

F. Computation of Actuator Shape

The actuator's equilibrium shape is obtained in response to the external forces and pressure by minimizing the net energy

TABLE II
GEOMETRIC PARAMETERS THAT CORRESPOND TO A SINGLE COMPOSITE
ACTUATOR (UNIT: MM)

L_x 110	$\frac{L_y}{31.75}$	L_c 20	C_x 105	$\frac{C_y}{26}$	H 8.2	$h_1 \\ 3.7$	h_2 1.8	h ₃ 2.1	$h_{3a} = 0.9$	
h_{3b} 1.1	$w_1 \\ 8.0$	$\frac{w_2}{6.0}$	t 2.0							

TABLE III

MATERIAL PROPERTIES AND THICKNESSES OF THE LAMINAE CONSIDERED FOR

MODELING AND FABRICATION

	Thickness (mm)	E_1 (MPa)	E_2 (MPa)	$\nu_1 = \nu_2$
Constraining layer (PP)	0.4	263	263	0.43
Fluidic layer (pure elastomer)	4.0	1.2	1.2	0.48
Regular EMC (reinforced elastomer)	2.0	1.5	170	0
Prestressed EMC	1.8	Nonlinear	170	0

using the variational Rayleigh-Ritz approach as

$$\frac{\partial(\sum_{1}^{N}\Phi_{(i)}) - \partial(\sum_{1}^{N}W_{P(i)}) - \partial W_{F}}{\partial k_{i}} = 0$$
 (21)

where $k_i = (b_{i1}, b_{i3}, c_{i1}, d_{i2}), i \in [1, ..., N]$, which results in 4N nonlinear algebraic equations. The 4N equations are calculated symbolically from (21), which are then solved numerically with the Newton–Raphson method.

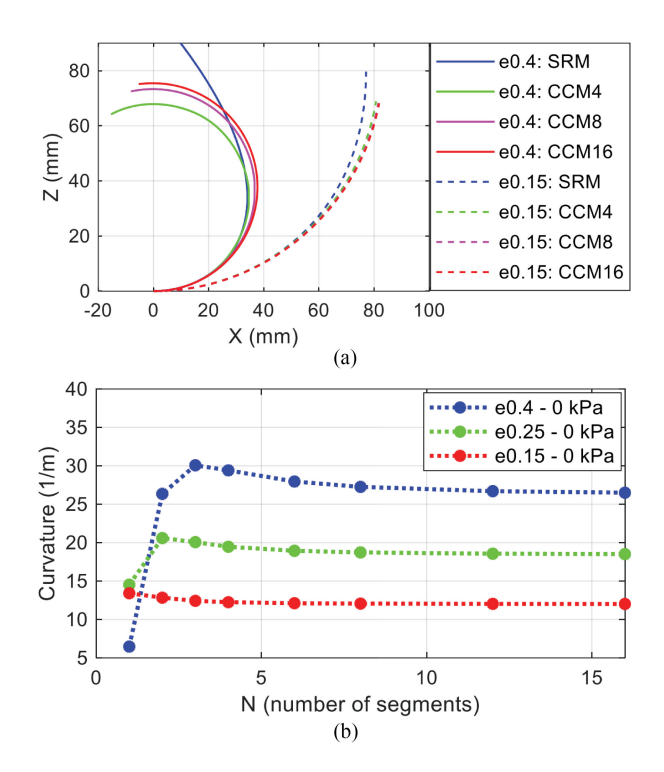
IV. MODEL-BASED STUDY OF FPC ACTUATOR RESPONSE

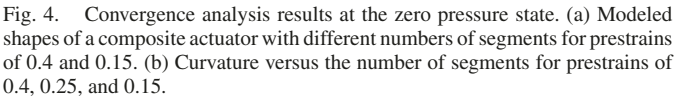
In order to determine the numbers of segments used in the CCM, a convergence study is conducted with different numbers of segments. Then, case studies are developed and conducted to optimize the design of a composite actuator and develop a thorough understanding of how different design parameters affect curvature, flexural rigidity, and actuation effort. A parametric study investigates the effects of design parameters, including prestrain and fluid channel size, on actuator response. The composite structure in Fig. 2 is considered with the dimensions and material properties shown in Tables II and III.

A. Convergence Study of Actuator Curvature

To study the effects of the number of segments N on the actuator curvature, the CCM is run for different numbers, including 1, 2, 3, 4, 6, 8, 12, and 16 segments. Here, N=1 represents a single segment, which equals the SRM. Three prestrains, 0.4, 0.25, and 0.15, are modeled for all numbers of segments. The value of the prestrain indicates how much the bottom EMC layer is prestretched. For example, 0.4 means the bottom EMC layer is prestretched to 1.4 times its original length before it is bonded to other layers. No load is applied and pressures are applied from 0 kPa with an increment of 27.6 kPa until the actuator curvature is almost zero (flat).

Fig. 4 shows the convergence analysis results at the zero pressure state. The modeled shapes of a composite actuator with four different numbers of segments for prestrains of 0.4 and 0.15 are illustrated in Fig. 4(a). It is observed that the prestrain of 0.4 has a much larger curvature than the prestrain of 0.15. The SRM with a prestrain of 0.4 does not yield a circular shaped like the CCM, and the SRM with a prestrain of 0.15 yields a slightly larger curvature than the CCM. With the new CCM,





each segment is represented by a low-order polynomial function. Therefore, the model will output a solution that does not have a constant curvature. Because we designed our actuators with a uniform construction along their lengths, they happen to have nearly constant curvatures. As a result, we use curvature as a simple metric for describing actuator shapes over the range of prestrains and pressures examined. In order to calculate the curvatures of the actuator, the modeled shapes are fit to circles using least squares, as shown in Fig. 4(b). For a prestrain of 0.15, it is observed that the SRM (N=1) yields a similar curvature as the CCM. For prestrains of 0.4 and 0.25, the SRM deviates significantly from the CCM since the SRM predicts shapes far from circular. All three curves tend to converge on constant curvature values as the number of segments is increased and indicate that using more than eight segments will have a minimal effect on the calculated curvature for the range of initial curvatures examined in this study.

Fig. 5(a) shows the curvature versus pressure for prestrains of 0.4, 0.25, and 0.15 modeled with 1 (SRM), 4, 8, and 16 segments. It is observed that the SRM fails at predicting larger curvatures and agrees with the CCM for smaller curvatures. For the CCM alone, CCM4 has a larger curvature than CCM8 and CCM16, and the difference decreases with increasing pressure. In summary, the larger the expected curvature, the more segments should be used in the CCM. As expected, the more segments that are employed, the more converged the model results.

Fig. 5(b) shows the computational time for a prestrain of 0.25 with no pressure or force. The initial conditions for the polynomial coefficients are set to be equal for all segment

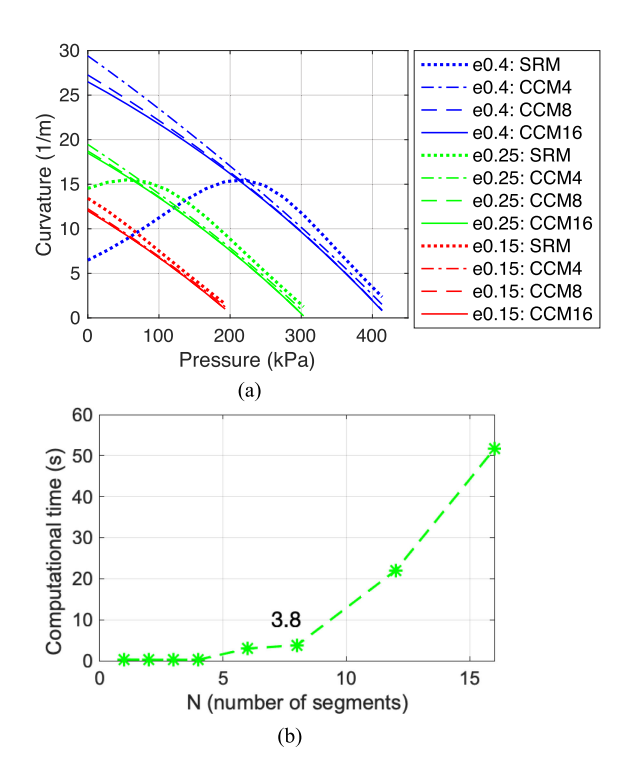


Fig. 5. (a) Curvature versus pressure for different prestrains and numbers of segments. (b) Computational time for a prestrain of 0.25 with no pressure or force.

numbers. The computational time is similarly low for segments less than or equal to 4 (0.2–0.3 s) but is much higher for 12 segments and above. CCM8 takes 3.8 s for this task. All results are computed in MATLAB using a MacBook (Retina, 12-in, Early 2015). Computational time varies little within the range of prestrains and pressures studied in this article. The number of segments is set to eight throughout the rest of this article due to relatively high accuracy and low computational time.

B. Parametric Study

For a given set of construction materials, prestrain and the width and height of the fluid channel have a major influence on the gripper's bending curvature, flexural rigidity, and actuation effort. The width and the height of the fluid channel are C_y and $h_{3a}+h_{3b}$, respectively. In the dimensional analysis, the values of Cy and h_{3a} are varied, and the rest of the dimensions are maintained as shown in Table II. Note that varying the lower fluid channel height h_{3b} has a similar effect on the actuator's response as varying the upper fluid channel height h_{3a} , which is not examined here.

The flexural rigidities of a composite actuator along the X and Z axes are defined in a similar way as for a cantilever beam

$$K_x = \frac{f_0 l_z^3}{3\delta_x}, \ K_z = \frac{p_0 l_x^3}{3\delta_z}$$
 (22)

where δ_x and δ_z are tip displacements in the X and Z directions caused by end loads f_0 and p_0 , respectively, at a fixed fluid pressure (see Fig. 6). The lever lengths l_z and l_x are the global positions along the Z and X axes in the loaded equilibrium

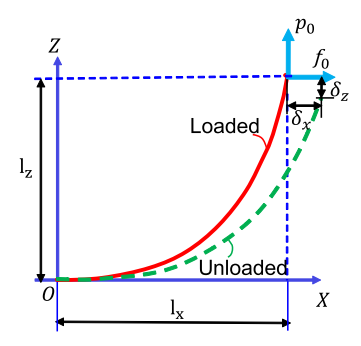


Fig. 6. External end forces applied on an initially curved composite actuator.

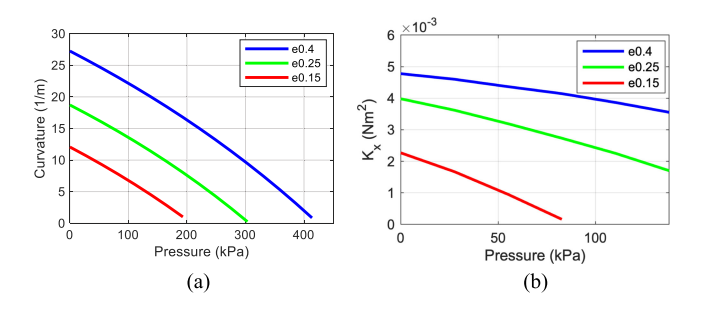


Fig. 7. Response of an FPC actuator for different prestrains with CCM8. (a) Curvature versus pressure. (b) Flexural rigidity along the *X*-axis versus pressure.

state, which are equal to W_{Ne}^0 and U_{Ne}^0 , as described in Section III-D. In this article, we use K_x for parametric studies since it approximately aligns with the grasping direction, which provides more information about grasping rigidity. To determine the flexural rigidity at a fixed pressure, we first run the CCM to find the unloaded equilibrium shape at that pressure. Next, δ_x is set equal to 10 mm to find f_0 and the loaded equilibrium shape at that pressure using the CCM. Then, K_x is calculated based on (22). All parametric studies are conducted with eight segments, CCM8.

Fig. 7 shows the response of an FPC actuator for different prestrains. The values of C_y and h_{3a} are maintained at 26 and 0.9 mm, respectively, as shown in Table II. It is observed that curvature versus pressure curves are almost parallel for different prestrains, and the higher the prestrain, the higher the curvature [see Fig. 7(a)]. To achieve a curvature of zero, higher pressures are needed for higher prestrains. Flexural rigidity K_x is found to decrease with increasing pressure, and the higher the prestrain, the larger the flexural rigidity [see Fig. 7(b)]. This is because higher prestrains have larger lever lengths l_z , which increase flexural rigidity according to (22). In addition, smaller prestrains have steeper slopes, which is because the term l_z^3 in (22) decreases faster for smaller curvatures. When the actuator is actuated to be fully flat, l_z is zero, which leads to $K_x = 0$.

The actuator response for different fluid channel widths C_y is shown in Fig. 8. The values of prestrain and h_{3a} are maintained at 0.25 and 0.9 mm, respectively. It is observed that increasing C_y reduces the actuation pressure needed to achieve the same curvature and flexural rigidity and increases the curvature in the unactuated state. This occurs because increasing the

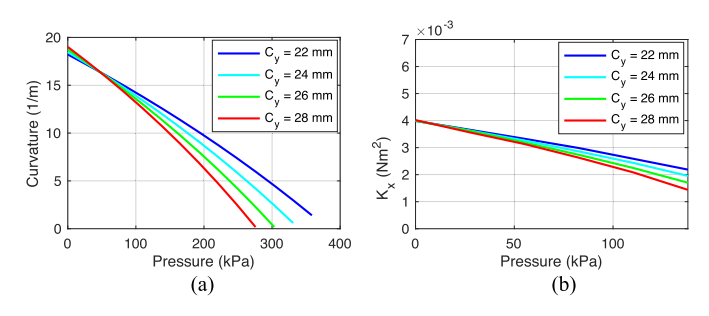


Fig. 8. Response of an FPC actuator to fluid channel width with CCM8. (a) Curvature versus pressure. (b) Flexural rigidity along the X-axis versus pressure

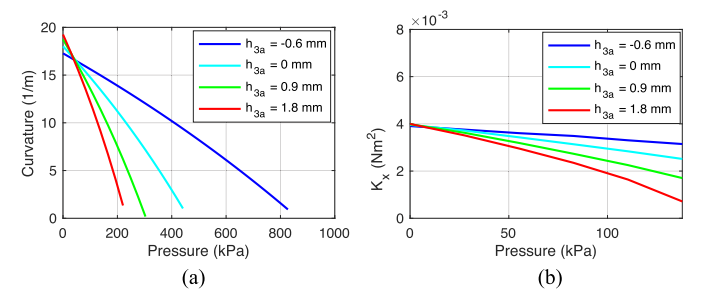


Fig. 9. Response of an FPC actuator to the upper fluid channel height with CCM8. (a) Curvature versus pressure. (b) Flexural rigidity along the X-axis versus pressure.

cross-sectional area of the fluid channel increases the available actuation energy at that pressure. In addition, the higher C_y , the more material reduction in the fluidic layer, the higher the curvature in the unactuated state. In general, increasing C_y leads to softer actuators but requires lower actuation pressure to flatten actuators and open up a gripper.

The prestrain and C_y are maintained at 0.25 and 26 mm, respectively, and the effects of the upper fluid channel height h_{3a} are modeled as shown in Fig. 9. Note that negative h_{3a} means that the fluid channel ceiling is below the actuator's midplane. It is observed that the slopes of both curvature and flexural rigidity curves increase with h_{3a} . This behavior is similar to varying Cy. The overall effect of increasing C_y or h_{3a} is increasing unactuated curvature, reducing flexural rigidity, but reducing actuation effort to achieve the same curvature or flexural rigidity.

Within a given actuation pressure range, the maximum curvature variation is obtained for $C_y \to L_y$ and $h_{3a} \to h_2$, which may cause extremely high strain at high pressure states due to extremely thin walls for the fluidic layer. Conversely, the minimum flexural rigidity variation within a given actuation pressure range is obtained for $C_y \to 0$ and $h_{3a} \to -h_{3b}$, which requires significant actuation effort to flatten the actuator. In addition, actuators with higher prestrains provide similar curvature variation and smaller flexural rigidity variation within a given actuation pressure range but require much more actuation effort to flatten. In the following study, we maintain C_y at 26 mm and h_{3a} at 0.9 mm since they generate relatively higher unactuated curvature and require relatively less actuation effort to achieve the same curvature or flexural rigidity.

V. ACTUATOR PROTOTYPING AND GRIPPER DEMONSTRATION

To experimentally validate the CCM, three sample composite actuators are fabricated with prestrains of 0.4, 0.25, and 0.15, respectively. The fabrication procedures for each layer and the FPC actuator are presented in Section V-A. Dimensions and material properties of the FPC actuator are shown in Tables II and III. Then, a soft gripper is constructed with three composite actuator fingers to demonstrate its capabilities, as described in Section V-B.

A. Actuator Prototyping

Each finger of the soft gripper is an FPC actuator fabricated with four laminae: a prestressed EMC, a fluidic layer, a regular EMC, and a constraining layer. The fabrication processes are presented in Fig. 10.

Fig. 10(a) shows the fabrication steps for a 90° EMC. Two silicone sheets are molded as shown in (i) and (ii). A layer of 90° carbon fibers is created by removing 0° fibers from a bidirectional woven carbon fiber fabric as shown in (iii) and (iv). Then, the EMC layer is made by sandwiching the 90° carbon fibers between two precured silicone layers using freshly mixed liquid silicone rubber, as shown in (v). Bluestar Bluesil V-340/CA 45 silicone rubber with shore hardness 45A is used as the elastomeric matrix and for the fabrication of all elastomeric elements in the composite actuators. The bidirectional woven 3-K carbon fiber fabric is from Fibre Glast Developments Corporation.

Fig. 10(b) illustrates the fabrication process for a fluidic layer. A layer of silicone is laid out on the base mold to form the bottom of the fluidic layer, as shown in (i). Molds for fluid channel, length adjustment, and walls of the fluidic layer are placed on the precured layer and base mold to form the fluid channel and the wall as shown in (ii). These molds are 3-D printed with an Ultimaker S5 using polylactic acid (PLA). If a different finger length is desired, the mold for length adjustment can be reprinted with a different size to easily change the finger length. A metal tube is used as a mold to form a round pressure supply channel with a diameter of 1.65 mm. Next, a paraffin wax mold is used to create ribs inside the air channel. The paraffin wax mold is made by casting wax into a 3-D printed polyvinyl alcohol (PVA) mold [(iii) and (iv)], which is dissolved by water when the wax becomes solid, as shown in (v). Then, the PLA mold for the fluid channel is removed, and the paraffin wax mold for the ribs is placed into the fluid channel. Fresh silicone is, then, poured into the mold to create the ribs inside the air channel and the top surface of the fluidic layer [(vi) and (vii)].

The fabrication steps for a composite actuator are demonstrated in Fig. 10(c). A polypropylene (PP) constraining layer with transverse ribs on one side is 3-D printed using an Ultimaker S5. To make the composite actuator, a cured 90° EMC layer is first stretched to the desired prestrain and held at its ends by two grips, as shown in (i). Then, the prestressed EMC and a regular EMC are bonded on either face of the fluidic layer using a silicone adhesive (DAP Auto-Marine 100% RTV silicone sealant), which takes 24 h to fully cure. Next, this intermediate composite is put in an oven at 60 °C to melt the wax out, and

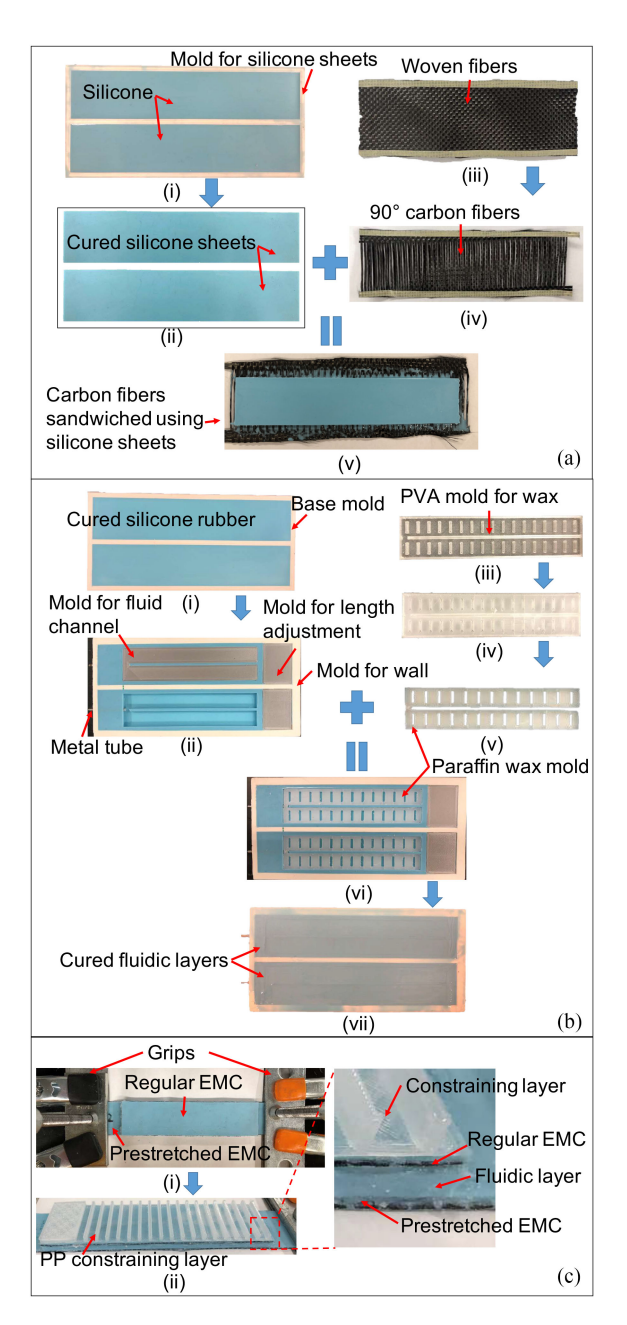


Fig. 10. (a) 90° EMC fabrication. (b) Fluidic layer fabrication. (c) Construction of a composite actuator to serve as a gripper finger.

then restretched to the desired prestrain by the grips at the ends. The constraining layer is bonded to the top of this three-layered composite using a cyanoacrylate adhesive (Loctite 681925), as shown in (ii). After the adhesive is fully cured, the mold for the pressure supply channel (metal tube) is removed, and a soft PVC tube (outside diameter 3.2 mm) is pushed into the round air supply channel [see Fig. 11(c)]. Since the diameter of the PVC soft tube is nearly twice as large as the molded supply channel, the channel exerts a high compressive force on the tube. This forms a tight bond and enables high pressure input without air leakage. A sample actuator with 0.4 prestrain is shown in Fig. 11, where the resulting composite has a curved shape in its equilibrium state and can be pressurized to vary curvature.

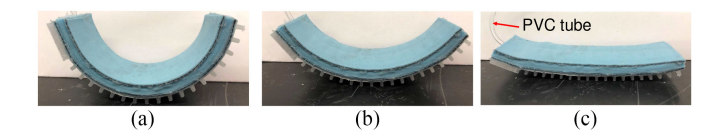


Fig. 11. Cured composite actuator with 0.4 prestrain. (a) Unactuated equilibrium state (0 kPa). (b) Actuated intermediate state (193 kPa). (c) Actuated almost-flat state (386 kPa).



Fig. 12. Demonstration of composite actuator gripper grasping a variety of objects.

B. Gripper Demonstration

A demonstration gripper is constructed with three composite actuators as fingers. Each composite actuator is fabricated with a prestrain of 0.25, and the dimensions are listed in Table II. These actuators are clamped by fixtures connected to a palm. The palm and fixtures are all 3-D printed with an Ultimaker S5 using PLA. When pressurizing the three actuators simultaneously, the gripper opens up to reach around objects. Releasing the pressure returns the actuators to their equilibrium unactuated states, hence closing the gripper and grasping an object. To demonstrate its capabilities, objects of various shapes are grasped by the prototype soft gripper, as shown in Fig. 12.

VI. EXPERIMENTS AND MODEL VALIDATION

Tests, including motion capture and loading, are performed on composite actuators to validate model accuracy. With accurate models for composite actuators under both small and large deflections, shapes and flexural rigidities can be predicted for different pressures and loading conditions.

A. Motion Capture Tests of Composite Actuators

Motion capture tests have been set up and performed on composite actuators to measure their shapes as a function of pneumatic pressure under quasi-static conditions, as shown in Fig. 13(a) and (b). Composite actuators with prestrains of 0.15, 0.25, and 0.40 are fabricated, and each is clamped to a fixture using bolts at its root. The actuators are pressured using a

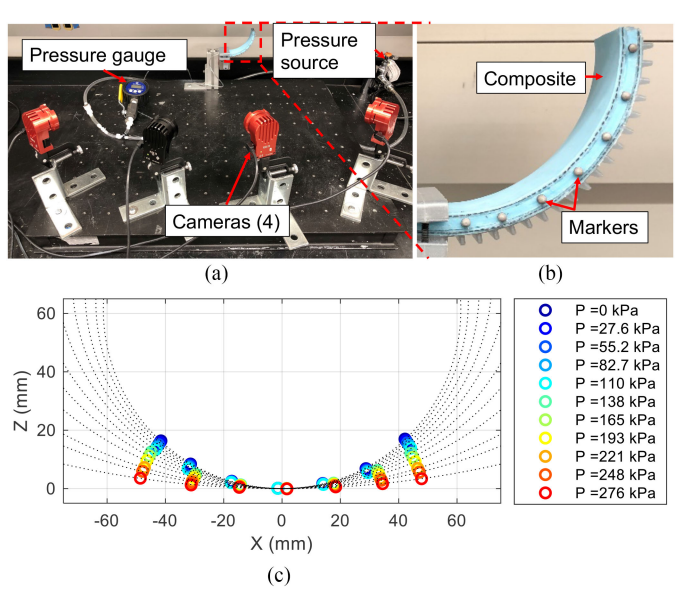


Fig. 13. (a) Motion capture test setup. (b) FPC actuator equipped with markers. (c) Measured coordinates of the markers for a composite actuator with a prestrain of 0.25 at different pressures.

laboratory compressed air system with a pressure gauge and a pressure regulator to measure and adjust the pressure. An OptiTrack motion capture system with four cameras (resolutions: 1.3 megapixels) is used to track reflective markers placed along the side of the actuator's midplane [see Fig. 13(b)]. To obtain the actuator curvature, the measured marker coordinates are fit to a circle using the least squares method [see Fig. 13(c)]. The fitted circles are plotted using black dotted curves in Fig. 13(c).

Using the large rotation model (CCM) described in Section III with eight equal-length segments, the modeled composite shapes (of the midplane) are obtained at different pressures for three samples with prestrains of 0.15, 0.25, and 0.4. The modeled shapes for the prestrain 0.25 case are compared to the experimental shapes in Fig. 14(a). In order to calculate the curvatures of the actuator, the modeled shapes are fit to circles using least squares, and the curvatures from the model are compared to those from experiments in Fig. 14(b). Here, the root-mean-square deviation (RMSD), which is the square root of the mean square error (MSE), is used to evaluate the circle fitting error for both experimental and modeled shapes in Fig. 14(c). For each shape, the MSE is calculated as the mean of the squared distance between the fitted circle and each point on that shape. It is noted that all RMSDs are significantly smaller than the fitted radius (inverse of curvature), indicating the good fit of the circles with constant curvature. The RMSDs for experimental shapes are, in general, larger than those for modeled shapes. This is because the modeled shapes are smoother than the experimental shapes, where only seven markers were used for motion capture tests. It is noted that the RMSDs for the modeled shapes increase with pressure for all prestrains. This behavior is due to the absence of an air channel inside the tip of the actuator, which has a slightly different curvature than the rest of the actuator that contains an air channel. The difference increases with pressure since the pressure does not morph the tip of the actuator. However, both the

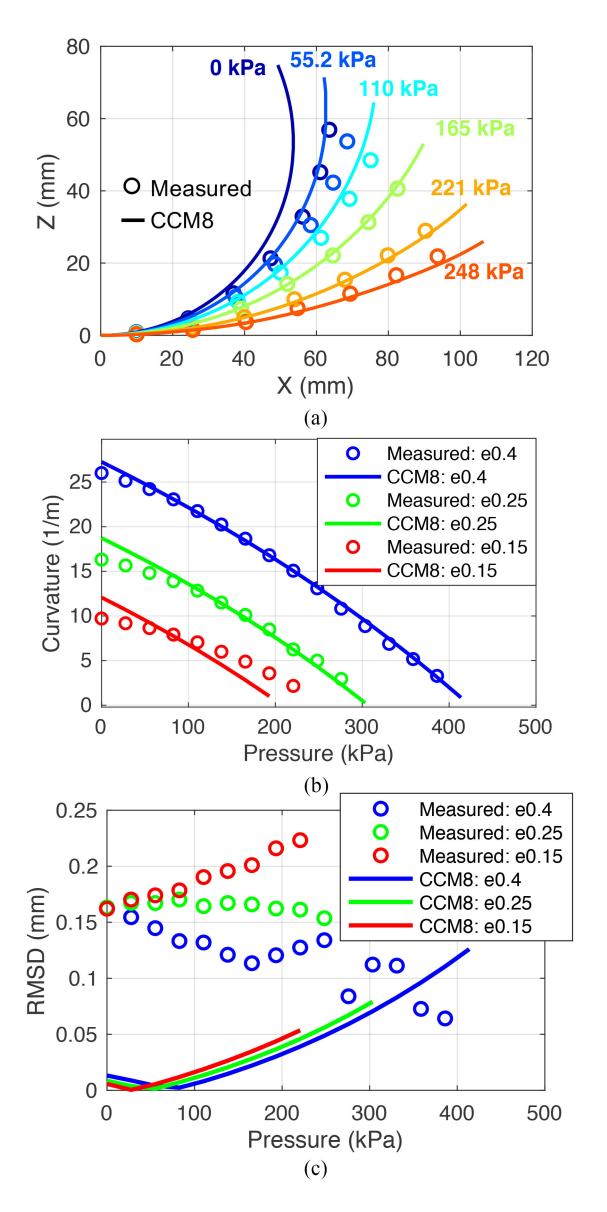


Fig. 14. (a) Comparison of shapes for a composite actuator with 0.25 prestrain from measurements and CCM8. (b) Comparison of curvatures of composite actuators from measurements and CCM8. (c) RMSD of least-squares-fitted circles for composite actuators from measurements and CCM8.

difference and the RMSDs are small enough to assume constant curvature for pure pressurization without loads. The RMSDs for the experimental shapes are different for different prestrains, which is mainly due to the imperfect alignment of the reflective markers.

In general, the measured quasi-static responses of the composite actuators match fairly well with the CCM8 results. A divergence is observed for 0.25 prestrain at low pressure states. This phenomenon may be caused by overpredicting curvature due to the plane stress assumption. In addition, the ribs inside the fluid channel have a cross-sectional area of 2×2 mm, which violates the small thickness assumption in classical theory of plates, where the thickness is assumed to be no greater than one-tenth of the smallest in-plane dimension. The longitudinal rib may contribute more to the divergence since it is aligned

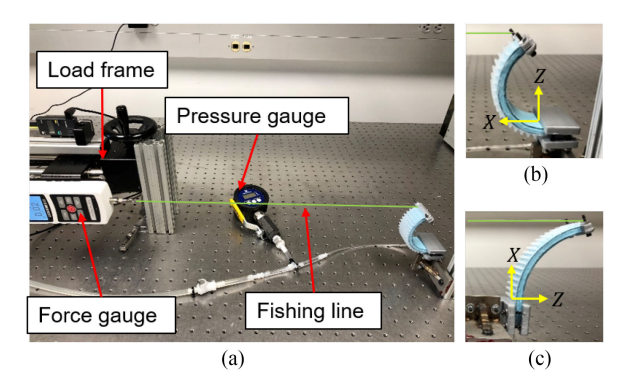


Fig. 15. (a) Experimental setup for bending tests. (b) Loading a sample with a prestrain of 0.4 in the X-direction. (c) Loading a sample with a prestrain of 0.15 in the Z-direction.

with the direction of curvature. This may reduce the bending flexibility and, hence, curvature. For 0.15 prestrain, it is also noted that the slope is larger for the modeled curvature-pressure curve. This may be because the extra energy needed for morphing thick ribs inside the fluid channel takes a larger portion of net energy for 0.15 prestrain than for larger prestrains. In addition, although the strain energy for the ribs in the constraining layer was found to be minimal and, thus, not modeled in the CCM, the presence of the thicker ribs concentrates the strain due to bending in the thin areas between ribs. This adds stiffness to the actuator, which may explain why the experimental curvatures at the zero pressure state for all prestrains are smaller than the modeled results in Fig. 14(b). However, ribs in the constraining layer cannot be modeled with the CCM since the ribs are thick (4 mm), which violates the plane stress assumption. The model could be modified to address these limitations with more advanced theories, such as first-order or third-order shear deformation plate theory for the analysis of relatively thick plates. In addition, the experimental samples may have some dimensional variability that would contribute to the divergence as well.

B. Loading Tests of Composite Actuators

Bending tests in both X and Z directions are performed to validate the analytical model under loading and internal pressurization conditions. A pressure gauge is used to measure the applied pneumatic pressure. A setup to measure tip forces for a composite sample is shown in Fig. 15. A Mark-10 ES20 load frame is used to apply a tip load to the free end of the prototype composite structure, while the tip load is measured with a Mark-10 ME-200 force gauge. The force gauge is connected with fishing line to an end fixture that is 3-D printed and attached to the free end of the composite actuator. In order to keep the fishing line straight, horizontal, and free of contact with the actuator except for the fixture, the Z-direction test must be performed using a sample with a smaller end slope, in which case samples with smaller prestrains are required. For the X-direction test, a sample with a higher curvature is preferred since the finger is more bent than drawn along its X-direction. If a flatter actuator is tested, it will result in more axial pulling than bending. Two samples with prestrains of 0.25 and 0.4 are

12 IEEE TRANSACTIONS ON ROBOTICS

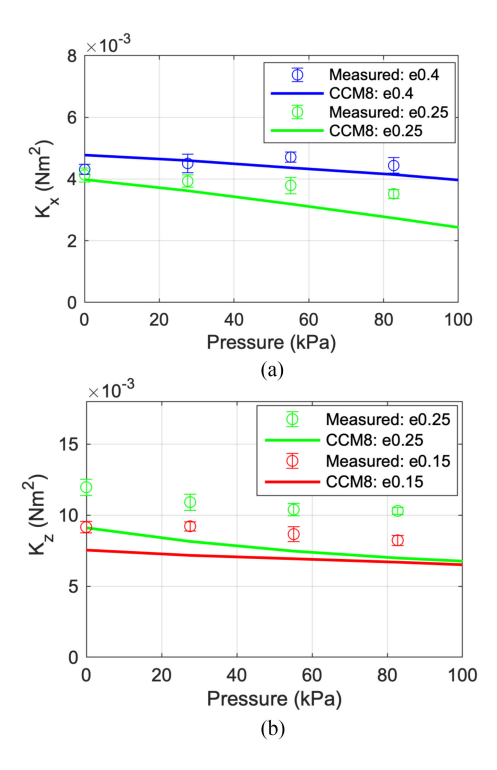


Fig. 16. (a) Flexural rigidity along the X-axis versus pressure. (b) Flexural rigidity along the Z-axis.

tested in the X-direction, and two samples with prestrains of 0.15 and 0.25 are tested in the Z-direction.

In order to determine the relationship between flexural rigidity and pressure, forces are measured at a selected displacement for a series of fixed pressures. The measurement procedure for each pressure state consists of four steps.

- 1) Apply a desired pressure with no load.
- 2) Pull the composite actuator towards the force gauge for 10 mm at that pressure and hold the actuator in the bent position.
- 3) Adjust the height of the actuator and align the actuator's endpoint with the measuring head of the force gauge.
- 4) Record the force.

Then, increase the pressure applied to the actuator by 4 psi (27.6 kPa) and repeat the four steps above. This is repeated for pressure states from 0 to 82.7 kPa. For each loading direction and pressure, bending tests are repeated five times to examine repeatability and to calculate the average value and standard deviation.

Flexural rigidities are calculated from (22) for the average measured forces and both displacements δ_x and δ_z equal to 10 mm according to the test procedure. The experimentally determined flexural rigidities are then compared to the flexural rigidities calculated from the CCM8 force results in Fig. 16. It is observed that the computational and experimental results for flexural rigidity K_x match fairly well for 0.4 prestrain. There is some divergence in K_x for 0.25 prestrain. The modeled flexural rigidities K_z exhibit similar trends as the experimental flexural rigidities but have larger values, indicating that the modeled actuators are softer than the physical samples. This is because assuming plane stress underpredicts bending forces and the ribs

in the constraining layer add extra stiffness to the actuator, which are not captured by our model. Higher model accuracy can be achieved by considering transverse stresses and including the ribs on the constraining layer into the model.

VII. CONCLUSION

This article introduced an analytical model called the CCM to model the quasi-static response of FPC actuators to different loading and pressure conditions for both small and large curvatures. The model eliminates the limitations of small deflections and constant curvatures, enables fast computation (200 ms to multiple seconds), and provides a solution for developing fingers for soft grippers.

A model-based parametric study was conducted to investigate the effects of parameters influencing curvature, actuation effort, and flexural rigidity. It was found that higher prestrains increase the equilibrium curvature and flexural rigidity. In addition, increasing fluid channel dimensions increases the equilibrium curvature and reduces flexural rigidity, but reducing actuation effort to achieve the same curvature or flexural rigidity.

FPC actuators were fabricated and shown to be able to withstand pressures of up to 400 kPa. A soft gripper was manufactured to demonstrate the grasping ability of the FPC actuators. Motion capture and loading experiments were set up and conducted to characterize the actuator response to pneumatic pressure and loads and to validate the CCM. The experimental and computational results matched fairly well, although there was divergence for some cases, which was likely due to the ribs inside the fluidic layer that did not meet the small thickness and plane stress assumptions, and the ribs in the constraining layer that added extra stiffness to the actuator. Higher model accuracy can be achieved by considering transverse stresses, using more advanced plate theories, and including the ribs on the constraining layer into the model.

Further efforts include design and modeling of gripper integration using current analytical models. With these models, the grasping capability of soft grippers composed of FPC actuators will be determined. In addition, smart soft grippers with embedded sensors will be investigated and developed. Further development of the analytical model and analysis of smart soft grippers would enable more precise control.

REFERENCES

- R. Deimel and O. Brock, "A novel type of compliant and underactuated robotic hand for dexterous grasping," *Int. J. Robot. Res.*, vol. 35, no. 1–3, pp. 161–185, 2016.
- [2] W. McMahan et al., "Field trials and testing of the OctArm continuum manipulator," in Proc. IEEE Int. Conf. Robot. Autom., 2006, pp. 2336–2341.
- [3] D. Trivedi, C. D. Rahn, W. M. Kier, and I. D. Walker, "Soft robotics: Biological inspiration, state of the art, and future research," *Appl. Bionics Biomech.*, vol. 5, no. 3, pp. 99–117, 2008.
- [4] S. Reitelshöfer, C. Ramer, D. Gräf, F. Matern, and J. Franke, "Combining a collaborative robot and a lightweight jamming-gripper to realize an intuitively to use and flexible co-worker," in *Proc. IEEE/SICE Int. Symp. Syst. Integr.*, 2014, pp. 1–5.
- [5] E. Brown et al., "Universal robotic gripper based on the jamming of granular material," Proc. Nat. Acad. Sci., vol. 107, no. 44, pp. 18809–18814, 2010

- [6] F. Ilievski, A. D. Mazzeo, R. F. Shepherd, X. Chen, and G. M. Whitesides, "Soft robotics for chemists," *Angewandte Chemie Int. Ed.*, vol. 50, no. 8, pp. 1890–1895, 2011.
- [7] R. K. Katzschmann, A. D. Marchese, and D. Rus, "Hydraulic autonomous soft robotic fish for 3D swimming," in *Experimental Robotics*. New York, NY, USA: Springer, 2016, pp. 405–420.
- [8] Y. Zhou, L. M. Headings, and M. J. Dapino, "Discrete layer jamming for variable stiffness co-robot arms," *J. Mech. Robot.*, vol. 12, no. 1, 2020, Art. no. 015001.
- [9] P. Polygerinos et al., "Soft robotics: Review of fluid-driven intrinsically soft devices; manufacturing, sensing, control, and applications in humanrobot interaction," Adv. Eng. Mater., vol. 19, no. 12, 2017, Art. no. 1700016.
- [10] B. Gorissen, D. Reynaerts, S. Konishi, K. Yoshida, J.-W. Kim, and M. De Volder, "Elastic inflatable actuators for soft robotic applications," *Adv. Mater.*, vol. 29, no. 43, 2017, Art. no. 1604977.
- [11] Y. Sun, Y. S. Song, and J. Paik, "Characterization of silicone rubber based soft pneumatic actuators," in *Proc. IEEE/RSJ Int. Conf. Intell. Robots Syst.*, 2013, pp. 4446–4453.
- [12] B. Tondu and P. Lopez, "Modeling and control of McKibben artificial muscle robot actuators," *IEEE Control Syst. Mag.*, vol. 20, no. 2, pp. 15–38, Apr. 2000.
- [13] R. F. Shepherd et al., "Multigait soft robot," Proc. Nat. Acad. Sci., vol. 108, no. 51, pp. 20400–20403, 2011.
- [14] V. Ho and S. Hirai, "Design and analysis of a soft-fingered hand with contact feedback," *IEEE Robot. Autom. Lett.*, vol. 2, no. 2, pp. 491–498, Apr. 2017.
- [15] Y. Li, Y. Chen, T. Ren, Y. Li, and S. H. Choi, "Precharged pneumatic soft actuators and their applications to untethered soft robots," *Soft Robot.*, vol. 5, no. 5, pp. 567–575, 2018.
- [16] V. S. Chillara, L. M. Headings, and M. J. Dapino, "Multifunctional composites with intrinsic pressure actuation and prestress for morphing structures," *Composite Struct.*, vol. 157, pp. 265–274, 2016.
- [17] A. D. Marchese, R. K. Katzschmann, and D. Rus, "A recipe for soft fluidic elastomer robots," *Soft Robot.*, vol. 2, no. 1, pp. 7–25, 2015.
- [18] M. Cianchetti, T. Ranzani, G. Gerboni, I. De Falco, C. Laschi, and A. Menciassi, "Stiff-flop surgical manipulator: Mechanical design and experimental characterization of the single module," in *Proc. IEEE/RSJ Int. Conf. Intell. Robots Syst.*, 2013, pp. 3576–3581.
- [19] K. M. de Payrebrune and O. M. O'Reilly, "On constitutive relations for a rod-based model of a pneu-net bending actuator," *Extreme Mech. Lett.*, vol. 8, pp. 38–46, 2016.
- [20] Z. Wang, Y. Torigoe, and S. Hirai, "A prestressed soft gripper: Design, modeling, fabrication, and tests for food handling," *IEEE Robot. Autom. Lett.*, vol. 2, no. 4, pp. 1909–1916, Oct. 2017.
- [21] G. Runge, M. Wiese, L. Günther, and A. Raatz, "A framework for the kinematic modeling of soft material robots combining finite element analysis and piecewise constant curvature kinematics," in *Proc. 3rd Int. Conf. Control, Autom. Robot.*, 2017, pp. 7–14.
- [22] J. Bishop-Moser and S. Kota, "Design and modeling of generalized fiber-reinforced pneumatic soft actuators," *IEEE Trans. Robot.*, vol. 31, no. 3, pp. 536–545, Jun. 2015.
- [23] S. D. Thomalla and J. D. Van de Ven, "Modeling and implementation of the McKibben actuator in hydraulic systems," *IEEE Trans. Robot.*, vol. 34, no. 6, pp. 1593–1602, Dec. 2018.
- [24] G. Gu, D. Wang, L. Ge, and X. Zhu, "Analytical modeling and design of generalized pneu-net soft actuators with three-dimensional deformations," *Soft Robot.*, vol. 8, no. 4, pp. 462–477, 2021.
- [25] R. J. Webster, III and B. A. Jones, "Design and kinematic modeling of constant curvature continuum robots: A review," *Int. J. Robot. Res.*, vol. 29, no. 13, pp. 1661–1683, 2010.
- [26] Q. Xie, T. Wang, S. Yao, Z. Zhu, N. Tan, and S. Zhu, "Design and modeling of a hydraulic soft actuator with three degrees of freedom," *Smart Mater. Struct.*, vol. 29, no. 12, 2020, Art. no. 125017.
- [27] S. H. Sadati, S. E. Naghibi, I. D. Walker, K. Althoefer, and T. Nanayakkara, "Control space reduction and real-time accurate modeling of continuum manipulators using Ritz and Ritz-Galerkin methods," *IEEE Robot. Autom. Lett.*, vol. 3, no. 1, pp. 328–335, Jan. 2018.
- [28] S. Sadati et al., "Reduced order vs. discretized lumped system models with absolute and relative states for continuum manipulators," in *Proc. Robot.* Sci. Syst. Conf., 2019, p. 10.

- [29] C. Della Santina, A. Bicchi, and D. Rus, "On an improved state parametrization for soft robots with piecewise constant curvature and its use in model based control," *IEEE Robot. Autom. Lett.*, vol. 5, no. 2, pp. 1001–1008, Apr. 2020.
- [30] M. W. Hyer and S. R. White, Stress Analysis of Fiber-Reinforced Composite Materials. Lancaster, PA, USA: DEStech, 2009.
- [31] J. N. Reddy, Theory and Analysis of Elastic Plates and Shells. Boca Raton, FL, USA: CRC Press, 2006.



Yitong Zhou received the B.Eng. degree in vehicle engineering from Tsinghua University, Beijing, China, in 2011, the M.Sc. and Ph.D. degrees in mechanical engineering, in 2016 and 2020, respectively, and the dual master's degree in applied statistic from the Department of Statistics from the Ohio State University, Columbus, OH, USA, in 2020.

In March 2021, she joined the Shien-Ming Wu School of Intelligent Engineering, South China University of Technology, Guangzhou, China, as an Assistant Professor. Her research interests include soft

robotics and mechanics modeling of materials and structures.



Leon M. Headings received the B.A. degree in physics from the Goshen College, Goshen, IN, USA, in 1999, and the B.S., M.S., and Ph.D. degrees in mechanical engineering from the Ohio State University, Columbus, OH, USA, in 1999, 2005, and 2011, respectively.

He is currently a Senior Research Associate with the Department of Mechanical and Aerospace Engineering, The Ohio State University. Prior to his graduate studies, he worked in passenger and light truck tire development with Bridgestone Americas,

Inc., Akron, OH. His research interests include modeling, characterization, development, and control of smart material devices and advanced manufacturing systems.



Marcelo J. Dapino received the Engineering Diploma from the University of Uruguay, in 1994 and the Ph.D. degree from Iowa State University, in 1999. He is the Honda R&D Americas Designated Chair in Engineering with the Ohio State University, Columbus, OH, USA, where he is also a Professor with the Department of Mechanical and Aerospace Engineering. He is the Director of the Smart Vehicle Concepts Center, a National Science Foundation Industry–University Cooperative Research Center. He has served as a Mechanical Engineering Educa-

tor and Primary Advisor for more than 80 graduate dissertations and theses, undergraduate theses, and postdoctoral associates. Along with his advisees and collaborators, he has authored or coauthored 130 archival journal articles, nine book chapters, and 120 conference papers and has generated 14 patents and intellectual property disclosures.

Prof. Dapino is a fellow of the American Society of Mechanical Engineers and the Society of Photo-Optical Instrumentation Engineers.